ZANCO Journal of Pure and Applied Sciences

TYPE Original article
DOI http://dx.doi.org/10.21271/ZJPAS.37.2.5

OPEN ACCESS

*Corresponding author

Ajay Kumar
ajay.tiwari1591@gmail.com

RECEIVED :10 /10 / 2024
ACCEPTED :08/03/ 2025
PUBLISHED :30/04/ 2025

KEYWORDS:

Electrically conductive papers (ECPs), Ferrite nanoparticles (FNPs), Nanocomposites (NCs), Cellulose paper (CP), Reduction, DC conductivity, Optical band gap (OBG)

Enhanced Electrical Conductivity of Graphite through Band Gap Reduction by Ferrite Nanoparticles

Ajay Kumar[1*], Shikha Aeron[2], Manish Pant[3], Hari Krishan[4], Saifullah Zaphar[5], Ankit Mittal[6], and Narinder Kumar[7]

[1]Department of Chemistry, School and Applied and Life Sciences, Uttaranchal University, Dehradun, Uttarakhand, India- 248007
[2]Department of CSE, Tula's Institute, Dehradun, Uttarakhand, India- 248197
[3]Department of Chemistry, DIT University, Dehradun, Uttarakhand, India- 248009
[4]Department of Chemistry, Michigan Diagnostic LLC, 2611 Parmenter Blvd, Royal Oak, MI, USA 48073
[5]Department of Renewable Energy and Efficiency, National Institute of Technology, Kurukshetra, Haryana, India-136119
[6]Department of Chemistry, Shyam Lal College, University of Delhi, Delhi-110032
[7]Department of Physics, Uttaranchal Institute of Technology, Dehradun, Uttarakhand, India- 248007

ABSTRACT

In this study, an effort was made to fabricate a series of electrically conductive papers (ECPs) by dispersing varying concentrations (%, w/w) of ferrite nanoparticles (FNPs, 8.27 nm) into a graphite matrix bind with hydroxypropyl methylcellulose (HPMC, 46.15%, w/w) and depositing this composite over cellulose paper (CP) (4 cm^2). FNP concentrations ranged from 1.0% to 3.0%. The surface characteristics of the ECPs were analyzed using SEM, while XRD was employed to confirm the crystallinity of the coating. The crystallite size of FNPs was calculated from the XRD data using the Scherrer equation. The effect of FNP addition on the thermal stability of the ECPs was also assessed. To confirm the semiconducting nature of ECPs, DC conductivity (σDC) was measured via the four-probe method. Additionally, diffuse reflectance spectroscopy was used to evaluate the effect of coating on the optical band gap (OBG) of the nanocomposites (NCs) over cellulose paper. Notably, FNPs significantly contributed to the reduction of the graphite-coated ECPs' band gap. This study presents a simple, reproducible method for fabricating and characterizing ECPs, highlighting their potential as electrodes for energy conservation and storage applications.

GRAPHICAL ABSTRACT

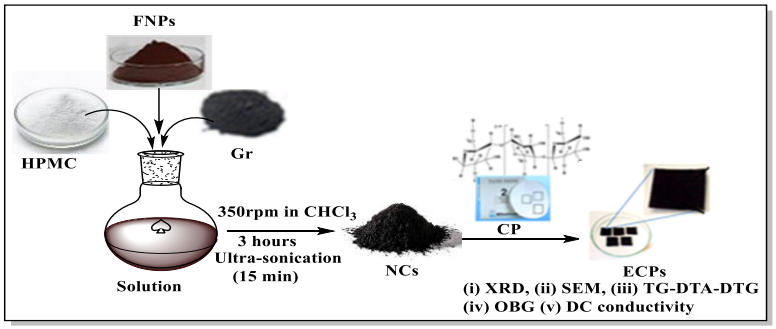

1.Introduction

The present century has witnessed the rapid use of devices for communication, entertainment, power and energy management, space, and biochemical research. To keep the devices functional, all their components must perform well. However, power and energy management in devices is prominent in making them functional over a long period. An electrode is an integral part of the system (Chang and Park, 2006). There has been substantial research on the fabrication of a variety of electrodes for different classes of devices (Wang et al, 2017). The best commercialization of electrodes is possible through reducing the cost-to-performance ratio of the electrode system. In the present work, efforts have been made toward the development and characterization of cellulose Electrically Conductive Paper (ECP) for their potential applications as anode electrodes for batteries (Lizundia et al, 2020; Oli et al, 2023), sensors (Liu et al, 2016), electromagnetic shielding (Zhang et al., 2021), and super-capacitors (Sheberla et al, 2017; Pereira et al, 2018; Lashkenari et al, 2023; Salama et al,2024).

The common substrates that are used for electrodes are metals (Hwang et al, 2008), quartz (Liang et al, 2010), silicon wafers (Sethuraman et al, 2012), mica (Peng et al, 2023; Li et al, 2017), plastic, etc. Plastics such as polyimide and polyester are used as substrates for developing conductive films in flexible electronics. Still, the disadvantage of using plastic as a substrate is that its large thermal expansion coefficients are mismatched with those of conductive materials. Hence, the conductive material over the plastic substrate will be spoiled by a change in temperature (*T*) (Nogi and Yano, 2009). For decades, graphite due to its ease of abundance, semi-conductivity, low cost, outstanding low expenditure, cyclic properties, electrochemical stability, and process ability has attracted as the most dominant electrode material (Amin et al, 2019; Ma et al, 2021) Several methods are used for the deposition of electrode materials: hand laying deposition, spin coating (Norrman et al, 2005), electrophoretic deposition (Boccaccini et al, 2006) which is commonly used in cyclic voltammetry. A hand-laying deposition is used for small system components and is applicable for fundamental testing. The goal is to find semiconducting materials that perform better than the standard electrode materials (Pollet and Kalanur, 2024; Ghimire et al, 2024). Cellulosic materials have recently received great attention as an optimistic alternative material due to their exclusive properties, such as biodegradability, flexibility, recycling possibilities, low cost, and light weight, in the field of portable and flexible electronics (Zhao et al, 2021). However, cellulosic fiber is non-conductive; its electrical conductivity depends upon the conductive fillers. The fillers, to make it electrically conductive, may be carbon black, carbon nanotube, graphene, carbon fiber, polyaniline, and polypyrrole as well (Devi et al, 2022; Sankaran et al, 2018; Kausar, 2018). Currently, ECPs are manufactured by either a wet-end formation or surface coating process. Surface coating is preferred over the wet-end formation process due to low cost, low-risk scale-up, and high filler retention (Tang et al, 2014). ECP can be used in Li-ion batteries as a current collector to replace the present metallic counterparts. The advantage of using paper as a substrate is that it improves film adhesion as compared to plastic (Hu et al, 2009). The eco-friendly preparation of ECP is still a challenging task.

A binder is another important component to satisfy the requirements of surface coating. Presently, polluting materials and commercial processes are being used in Li-ion technology, e.g., Poly vinylidene-di fluoride (PVdF), which is the most common polymeric binder for the fabrication of battery electrodes (Gutiérrez et al, 2023). For the processing of PVdF, toxic and volatile solvents are used, e.g., N-methyl-pyrrolidone, which is expensive and difficult to recycle at the end of battery life (Jeong et al, 2012). Eco-friendly materials, low-pollution generation, and recycling processes are being discovered. The biodegradable polymers, e.g., polyelectrolytes like cellulose, cellulose derivatives, and gelatin, which are electrically inactive and eco-friendly, support modifying the electrochemical behaviour of anode material (Hina et al, 2024; Kasprzak et al, 2022). These polymers are on the way to being a part of next-

generation materials from academic research to industrial invention. When an aqueous solution of these materials is treated with graphite, adsorption of graphite molecules occurs on their surface (Ji et al, 2013; Ivancev-Tumbas et al, 2020). These polymers have a notable impact on anode passivation and function as binders (Li et al, 2021). Transition metal oxides can also act as potential electrode material for Li-ion materials (Zhao et al, 2016). Among these, Fe_3O_4 shows eco-friendliness, low cost, high capacity, and natural abundance (Zhou et al, 2010). Ferrites' unique electrical and magnetic properties make them interesting materials for research and technological applications (Nongjai et al, 2012) such as electronic communication devices, sensors, magnetic storage, etc (Hashim et al, 2018). The development of nanotechnology has introduced the exploration of applications of ferrites in different areas (Rana et al, 2021; Qin et al, 2021). Magnetite is generally studied by combining with conductive carbon, such as carbon black, carbon nanotubes, graphite, and acetylene black, to enhance the electrical conductivity of electrodes (Nawwar et al, 2019; Bruck et al, 2016; Zhang and Ran, 2021; Sumdani et al, 2022; Anwar et al, 2023).

2. Material and Method

The present investigation deals with the formulation of ECPs by hydroxy propyl methyl cellulose (HPMC) with graphite in various concentrations of ferrite nanoparticles (FNPs) deposited over cellulose paper (CP) was characterized through UV-Vis, X-Ray Diffraction (XRD) spectra, Scanning Electron Microscopy (SEM), and simultaneous Thermo Gravimetric-Differential Thermal Analysis- Derivative Thermo Gravimetry (TG-DTA-DTG). The effect of FNPs on the DC Conductivity (σDC) of ECPs was investigated at room temperature (*T*) through a four-probe method at variable compliance of voltages. Graphite was procured from Loba Chemie Pvt. Ltd., Mumbai. Ferrous chloride tetrahydrate ($FeCl_2.4H_2O$) with molecular mass 198.91 was purchased from 'Molychem' Mumbai. HPMC was procured from 'Otto Chemie India'. Whatman filter paper no. 2 was procured from Sonex®. The rest of the chemicals and solvents were provided by the Department of Chemistry in >98 % purity and used without further purification.

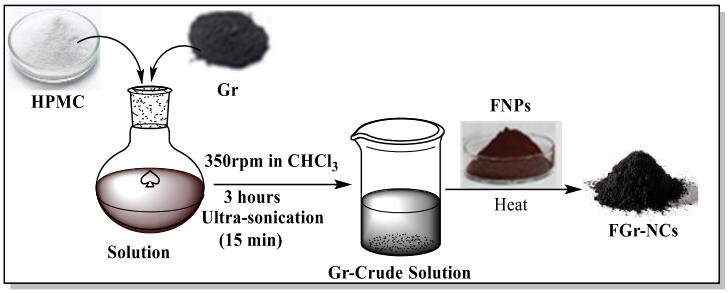

Figure 1 Synthesis of FGr-NCs

2.1 Preparation of Ferrite Nanoparticles (FNPs)

FNPs were prepared by dissolving $FeCl_2.4H_2O$ (3 g) in deionized water (100 mL) under vigorous stirring at 80 ºC. NH_4OH (50 mL,7.0 M) was added to the content at the rate of 0.33 mLs^{-1} drop by drop. A brown precipitate was formed in the initial stage of the reaction, which was dried at room temperature (*T*) in air overnight to obtain FNPs (Tashakkorian et al, 2022).

2.2 Development of Electrically Conductive Paper (ECP) without FNPs

ECPs were prepared with slight modifications to the method developed by Tang et al., 2014. Whatman filter paper no. 2 was used as the substrate, which was cut into a 2×2 cm^2 area using scissors. Coating materials were prepared through stirring a mixture of hydroxy propyl methyl cellulose (HPMC) (150 mg) and graphite (Gr) (175 mg) @ 350rpm in $CHCl_3$ (6.5mL) for 3 hours, followed by ultra-sonication of 15 minutes. The suspension (250μL) was then applied over cellulosic paper and left at room temperature (*T*), followed by drying at 40℃/400 mm Hg.

2.3 Development of Electrically Conductive Paper (ECP) with FNPs

Then, FNPs were added to the abovementioned solution with different concentrations to form nanocomposites (NCs), and NCs suspension (250μL) was applied over cellulose paper at room

temperature (*T*), followed by drying at 40℃/400 mm Hg. In the process, three ECPs were created using three distinct FNP concentrations. FNPs (1%) were added to the solution of HPMC and Gr to form ferrite graphite NCs (Figure 1), then after NCs coated over CP to form ferrite-graphite electrically conductive paper (FGr-ECP (I)). Similarly, 2% of FNPs have the same process as FGr-ECP (II), and 3% of FNPs have the same process as FGr-ECP (III) (Figure 2) (Lizundia et al, 2020).

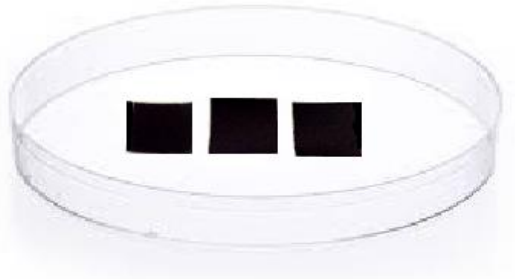

Figure 2 Fabricated FGr-ECP

2.4 X-ray Diffraction (XRD)

XRD was conducted over 'Rigaku Smart Lab X-ray diffractometer' using Cu-K_α radiation of wavelength λ= 0.154 nm in the range of 10º-90º. X-ray pattern was used to determine the crystallite size (D) by using Scherrer's formula **(**Scherrer, 1918; Fatimah et al, 2022) given by

$$D = \frac{k\lambda}{B\cos\theta} \quad \ldots(1)$$

where B is the full width at half maximum and k is a constant with a value of $2\,(\ln 2/\pi)^{1/2} = 0.93$.

2.5 Scanning Electron Microscopy (SEM)

The SEM images of fabricated ECPs were recorded on 'JEOL JSM 6610 LV' by using a primary beam voltage of 10 kV at 0.2 KX (10μm). The images were recorded under alike conditions for comparable results.

2.6 Thermal Characterization

Studying a material's thermal decomposition is useful in predicting its thermal stability. This can be examined using thermal gravimetric analysis (TGA), differential thermal analysis (DTG), and derivative thermal analysis (DTA). Simultaneous TG-DTA-DTG was conducted over EXSTAR TG/DTA 6300 for the sample weight of 10.52 mg at 10℃/min in the air at a flow rate of 200 mL/min with a temperature (*T*) ranging from 29 to 1000 ºC.

2.7 Optical Study

UV-Vis spectra of all the samples were taken by a Perkin Elmer Lambda 365 UV-Visible spectrophotometer in the wavelength range of 200-800 nm in reflectance mode. UV-Vis diffuse reflectance spectroscopy was employed to determine the samples' optical band gaps (OBGs) using the Kubelka-Munk (K-M) method.
The optical band gap (OBG) is evaluated using the Tauc equation (Tauc, 1974), which is expressed as

$$\alpha h\upsilon = K(h\upsilon - E_g)^n \quad \ldots(2)$$

where K is the constant of proportionality, α is the molar absorptivity, and E_g is the energy band gap of the sample. Here, 'n' can have four values: 1/2, 3/2, 2, and 3 for allowed direct, forbidden direct, allowed indirect, and forbidden indirect electronic transitions, respectively. While the determination of OBG using the Kubelka-Munk function (F(R)) offers great advantages. The K-M function is given as,

$$F(R) = \frac{(1-R)^2}{2R} \quad \ldots(3)$$

where R denotes reflectance. This relation generally applies to highly light-absorbing particles and scattering materials in a matrix (López and Gómez, 2012). F(R) is proportional to α. By plotting 'hu' as a function of $(F(R) \times hu)^n$ and then extrapolating the linear part of the curve to the 'hu' axis, the OBG can be obtained.

2.8 DC Electrical Conductivity Measurement

σDC of ECP was recorded over a Keithley four-probe conductivity meter equipped with a current source (6221DC) and nanovoltmeter (2182A) at

varying voltage (1V to 100V). All conductivity data were recorded at room temperature (*T*). A series of ECPs were fabricated through the dispersion of varying concentrations (%, w/w) of FNPs into a matrix of graphite (Gr) bound with HPMC (46.15%, w/w) followed by deposition over CP (4 cm^2). The FNP concentrations used for this purpose ranged from 1.0 to 3.0. The characterization of the ECP surface investigated the crystallinity through SEM and XRD of CP, FNPs, and FGr-ECP. The impact of FNP addition on ECP's thermal stability was investigated. To determine if ECP is semiconducting, the OBG of the coating was examined using the Tauc equation, and the σDC of ECP was examined using four probing techniques. The semiconducting properties of synthesized ECP revealed a qualitative correlation between OBG and σDC results.

3. Result and Discussion

3.1 Crystallinity

The XRD spectrum of cellulose paper is presented in Figure 3 (Ma et al, 2017). XRD indicates the characteristic peaks of cellulose paper; the most intense peak is observed at 2θ =22.50, and others at 26.63, 28.52, and 30.77 are small peaks. The crystallite size is 27.06 nm Figure 3 (a) (Costa et al, 2014). The calculations based on the Debye-Scherrer equation FNPs presented reveal a 16.93 nm crystallite size Figure 3 (b). XRD indicates the characteristic peaks of FNPs at 2θ =35.51, 43.13, 50.62, 57.50, and 63.09. This corresponds to the inter-planar spacing (reflections) of FNPs at 2.52 (311), 2.09 (400), 1.80 (422), 1.55 (511), and 1.47 (440), which indicate the cubic nature of FNPs. Calculations based on the Debye Scherrer equation reveal a 7.85 nm crystallite size of FNPs at 35.51. Consistency in the crystallite size of FNPs was marginally retained to 8.83 nm at 63.09° and 5.82 nm at 43.13°. However, a crystallite size of 10.59 nm was dominant with an interplanar distance of 1.47 Á at 63.09º. XRD data reveals the mean crystallite size of FNPs to be 8.27 nm (Jain, 2022). Non-uniform crystallite size reveals that FNPs are anisotropic. Intense sharp peaks in the XRD pattern of the Gr crystalline phase, the most intense peak in Gr, are observed at 2θ=26.50°, revealing its crystallite size as 30.79 nm (TODICA et al, 2014). FGr-ECP [III] demonstrates the presence of a crystalline phase. In the XRD pattern of FGr-ECP [III], the most intense peak is observed at 2θ=26.74°, attributed to a crystallite size of 33.37 nm Figure 3 (c) (Verma et al, 2021).

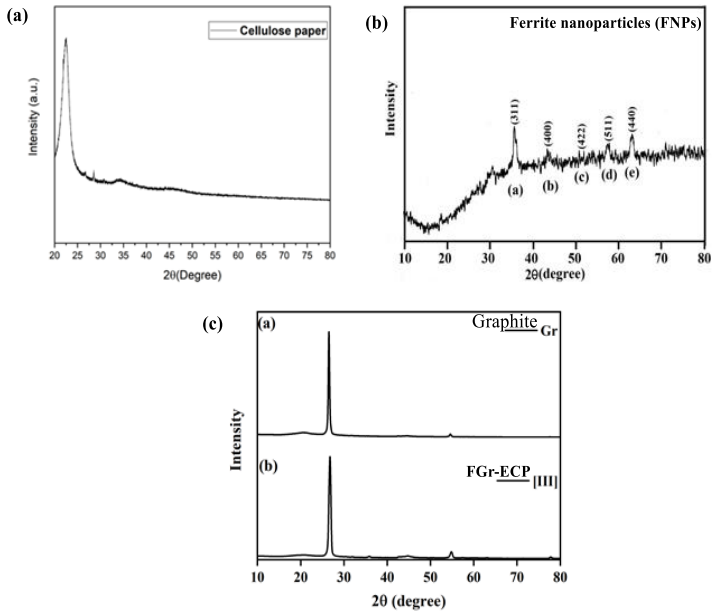

Figure 3 (a) XRD pattern of Cellulose Paper, (b) XRD pattern of FNPs, (c) XRD pattern of (a) Gr and (b) FGr-ECP [III]

3.2 Morphology

In Figure 4 SEM image represents the morphology of CP, Gr coated CP, and Gr modified with 3% of FNPs coated CP, abbreviated as ferrites Gr coated electrically conducting paper (FGr-ECP [III]), and represents the image of (d) at a higher magnification of 5KX, 5µm of the same (FGr-ECP [III]). Figure 4 (a) reveals the characteristic cellular morphology of CP (Mani et al, 2019). CP was fully covered through the coating of Gr Figure 4 (b) (Zhang et al, 2012). The dispersion of 3% FNPs has tarnished the smooth morphology of Gr into phase-separated agglomerated morphology. However, increasing magnification from 10KX, 10 µm to 5KX, 5µm presents a smooth morphology of FGr-ECP [III] Figure 4 (c). Microanalysis reveals the proper stable coating of FGr NCs

over CP that was found homogeneous at 5KX, 5µm Figure 4 (d).

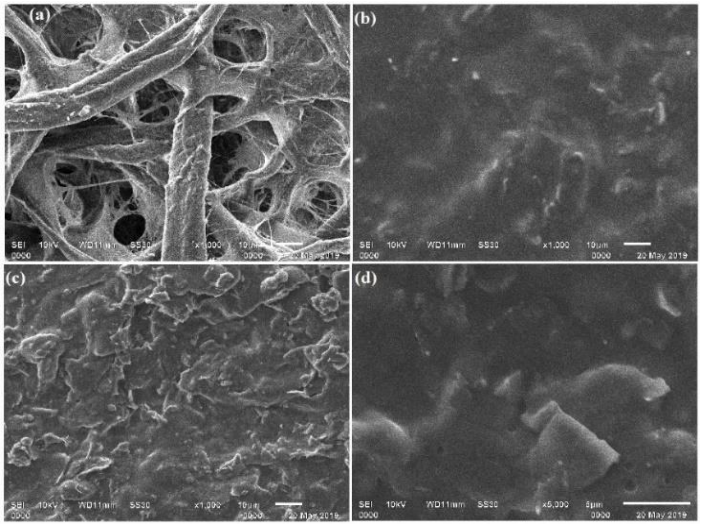

Figure 4 SEM images of (a) CP, (b) Gr-ECP, (c) FGr-ECP [III] (1KX, 10µm), and (d) FGr-ECP [III] (5KX, 5µm).

3.3 Thermal Stability

The thermal stability of NCs was assessed using TG-DTA-DTG in the air at a scan rate of 10 ^{o}C min^{-1}. Figure 5 represents the thermogram of Gr and FGr-ECP [III]. The thermal decomposition of NCs has been described in terms of TG weight residue (%Wr) of the samples left at temperature *T* (^{o}C) (Han et al, 2016; Zygouri et al, 2022). The enthalpy of decomposition (ΔH, mJg^{-1}C^{o-1}) is expressed as DTA endotherm (µV) at a peak temperature of *T* (^{o}C). The rate of decomposition is expressed in terms of DTG (mg/^{o}C) at a peak temperature of *T* (^{o}C). To express the comparable results, separate sketches of TG, DTA, and DTG are shown in Figure 5 (a, b, and c), respectively. The respective thermal data has been consolidated and is shown in the appendixes in (Table 1).

A coating comprising Gr in the presence of HPMC (46.15 %, w/w) as a binder reveals a marginal thermal decomposition till 214 ^{o}C, leaving 97.40 % Wr. The marginal weight loss of 2.60% w/w by coating is attributed to the expulsion of moisture and solvents contaminated during the preparation and processing of the coating. This has been supported with a weak DTA signal of 43.90 at 300 ^{o}C. DTG reveals the expulsion of extraneous contamination at the rate of 0.077 at 297 ^{o}C. TG at 214 ^{o}C has served as the onset for coating that rapidly reached 326 ^{o}C, leaving 63.60 % Wr.

Table 1: Thermal Characteristics Gr and FGr-ECP [III] NCs.

NCs	TG(On-set, ^{o}C) [W_R %]	TG(End-set, ^{o}C) [W_R %]	DTA (^{o}C) µV	-ΔH (mJg^{-1}C^{o-1})	DTG (^{o}C) [Rate: mg/^{o}C]
Gr	214[97.40] 326[63.60] 587[37.00]	326[63.60] 587[37.00] 664[1.80]	300[43.90] 401[80.80] 621[457.60]	0.32 0.76 7.47	297[0.08] 403[0.02] 616[0.64]
FGr-ECP [III]	218[99.00] 306[87.80] 552[81.40]	306[87.80] 552[81.40] 831[2.10]	- - 554 [0.22]	- - 11.50	280[0.02] - 707[0.06]

A major activity of thermal decomposition of the coating has appeared in the range of 326 to 612 ^{o}C. The coating slowly decomposed in the temperature (*T*) range of 326 to 587 ^{o}C, leaving 37.00 % Wr. In TG reveals a transient end set at 326 ^{o}C, leaving Wr of 63.6 % with a weak DTA signal of 83.40 at 401 ^{o}C. The decomposition of the coating progressed at the rate of 0.021 at 403° C. The transient end set appeared at 587 ^{o}C with a Wr of 37 % and was supported with an intense DTA signal of 457.60 at 621 ^{o}C. This has progressed with a rate of degradation of 0.60 at 616 ^{o}C. Beyond the transient end set of 587 ^{o}C, the coating was rapidly decomposed till 664 ^{o}C, leaving char residue of 1.8%, w/w. FGr-ECP [III] derived coating over ECP reveals higher TG onset, end set temperatures, DTG, and DTA peak temperatures over Gr coating containing 46.15 % HPMC. No significant decomposition of FGr-ECP [III] was observed till 218 ^{o}C. A marginal decomposition of FGr-ECP [III] was observed from 218 to 306 ^{o}C, leaving 87.80 % Wr. This progressed at the rate of 0.02 at 280 ^{o}C. Further, an increase in temperature from 306 to 552 ^{o}C imparts a marginal weight loss in FGr-ECP [III] by 6.40 %, w/w. The major decomposition of FGr-ECP [III] was observed in

the 552 to 831 ^{o}C range with respective residual weights of 81.40 and 2.10 %. This range of decomposition was associated with a broad DTA signal of 0.22 at 554 ^{o}C, along with the heat of decomposition of -11.50. This has progressed with DTG at the rate of 0.06 at 707 ^{o}C Figure 5 (a-c). The corresponding data has been tabulated in (Table 1). Thermal characteristics reveal the potential of FNPs to modify the stability of NCs. This further implies the development of thermally stable ECPs.

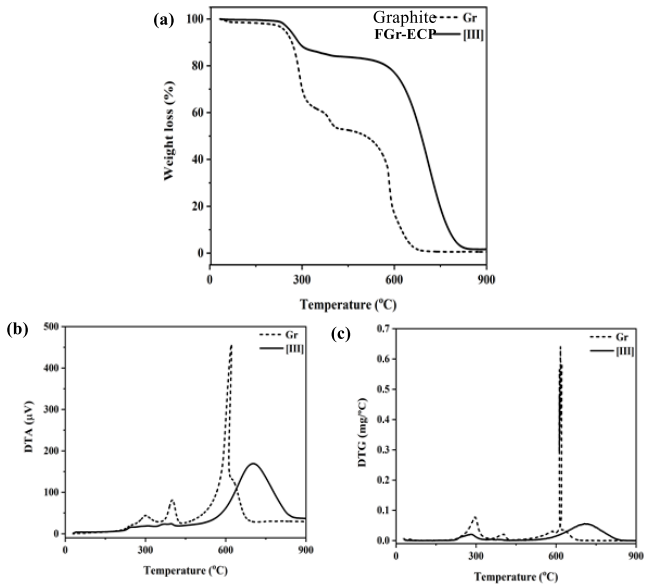

Figure 5 (a): TG of Gr and FGr-ECP [III]; (b): DTA of Gr and FGr-ECP [III]; (c): DTG of Gr and FGr-ECP [III]

3.4 Conducting Behaviour

To investigate the conducting behaviour of ECPs, they were examined for four probe-based voltage-regulated I-V and σDC. Respective data of σDC has been tabulated in (Table 2). All four probe experiments were conducted at selected voltages of 1V, 10V, and 100V. A linear I-V trend was observed which indicates the ohmic nature σDC was found to increase with voltage and concentration of FNPs σDC of the FGr-ECP [III]. Abnormal high σDC of CP is due to hydroxyl functionalities that make it hygroscopic and polar. Gr is devoid of polar functionalities that impart weak electrical conductivity over CP. However, the conducting nature of FNPs has raised σDC of Gr in proportion to the concentration that was further found to be functional with voltage in increasing order.

Table 2: Effect of voltage on conductivity at room temperature.

Samples	σDC $\times 10^{-3}$ (S.cm^{-1})					
	1V	Avg.	10 V	Avg.	100 V	Avg
CP	4.51 4.53 4.59	4.54	4.79 4.83 4.88	4.83	6.69 6.85 6.83	6.79
Gr-ECP	3.48 3.49 3.48	3.48	3.56 3.59 3.58	3.58	5.34 5.39 5.39	5.37
FGr-ECP [I]	3.70 3.74 3.76	3.73	3.88 3.86 3.88	3.87	5.77 5.88 5.88	5.84
FGr-ECP [II]	4.46 4.47 4.47	4.47	4.58 4.56 4.66	4.60	8.74 8.95 8.98	8.89
FGr-ECP [III]	5.10 5.16 5.11	5.12	5.24 5.22 5.22	5.23	11.20 11.40 11.10	11.23

The highest σDC ranging from 5.12 to 11.23 $\times 10^{-3}$ S.cm^{-1} was shown by FGr-ECP [III] at a voltage ranging from 1V to 100V Figure 6.

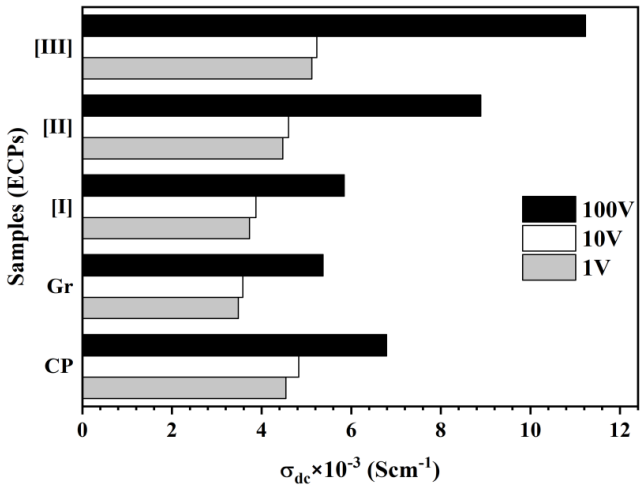

Figure 6: Variation of σDC of FGr-ECP [III] at different voltages

3.5 Optical Study

Diffuse Reflectance Spectroscopy (DRS) was applied to study the optical properties of prepared ECPs. The reflectance spectrum of FNPs Figure 7 has shown a broad reflection band between 247 nm and 705 nm, which shows good consistency with the literature (Chan et al, 2015; Singh and Yadav, 2020).

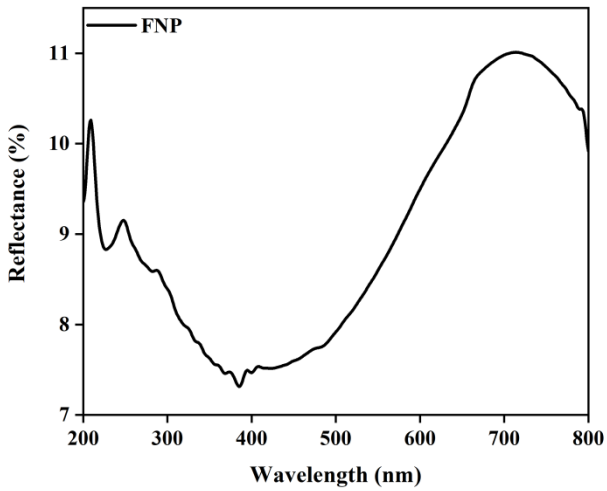

Figure 7: Diffuse Reflectance Spectra of FNPs

In the UV-Vis reflectance spectra of CP and various concentrations of ferrites in Gr-ECPs Figure 8 (Mund et al, 2021). The respective direct and indirect OBG are tabulated in (Table 3). Since σDC is found to be increasing with increasing FNP content, there must be a decrease in the OBG of ECPs. When FNPs are integrated with Gr, they create strong interfacial interactions. These interactions lead to the formation of surface and interface defects, which introduce sub-band energy levels within the band structure of Gr. This phenomenon effectively reduces the overall band gap (BG) of the NCs material. The interaction of FNPs with Gr enhances charge mobility across the hybrid material, thereby increasing electrical conductivity. Gr has a high surface area, and sp^2-bonded carbon structure provides an excellent platform for anchoring FNPs. This combination improves carrier hopping and electron mobility, further enhancing conductivity. The magnetic properties of ferrites combined with the dielectric properties of Gr contribute to better electromagnetic interference shielding and enhanced electrical properties in composite materials. Gr material, having high electron mobility and sp^2 hybridized structure, provides a platform for efficient charge separation. FNPs grafted onto graphene nanosheets reduce electron-hole recombination by capturing photo-generated electrons, which further minimizes energy losses and effectively reduces the band gap (Ahmed et al, 2024).

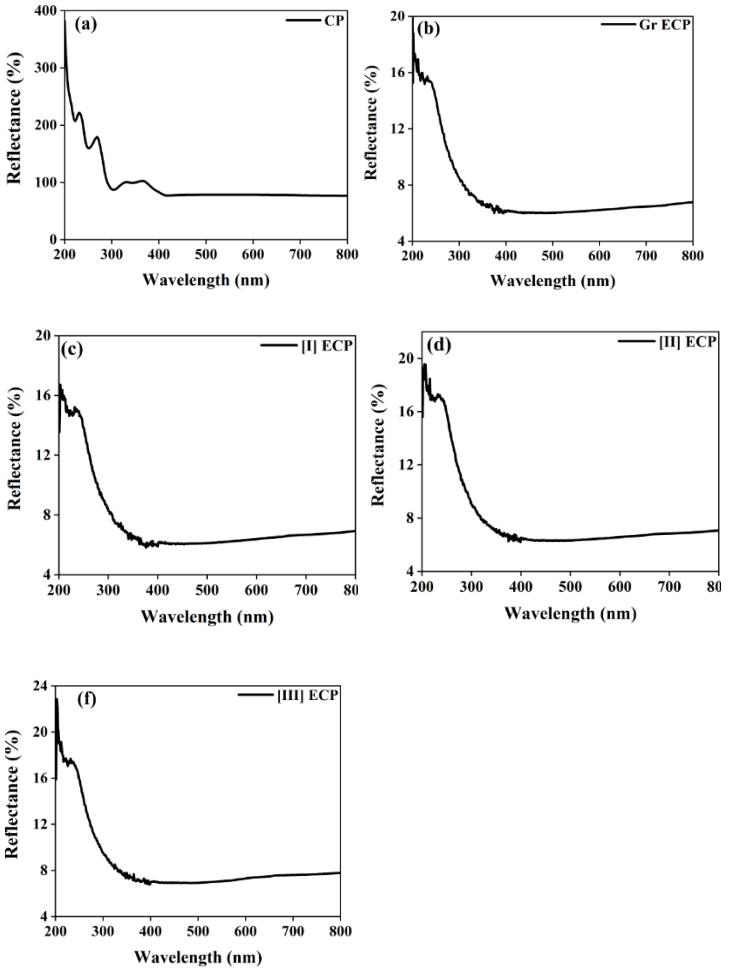

Figure 8: Diffuse Reflectance Spectra for (a) CP, (b) Gr-ECP, (c) FGr-ECP [I], (d) FGr-ECP [II] and (e) FGr-ECP [III].

In Figure 9 (Jalil et al, 2017) and Figure 10 present the plot of hυ v/s $(F(R)\ h\upsilon)^{n}$ to determine direct OBG (n=2) and indirect OBG (n=1/2).

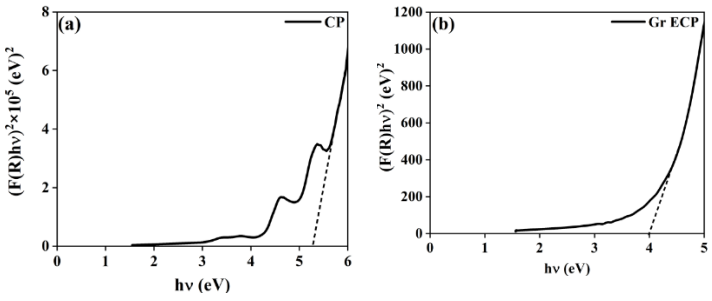

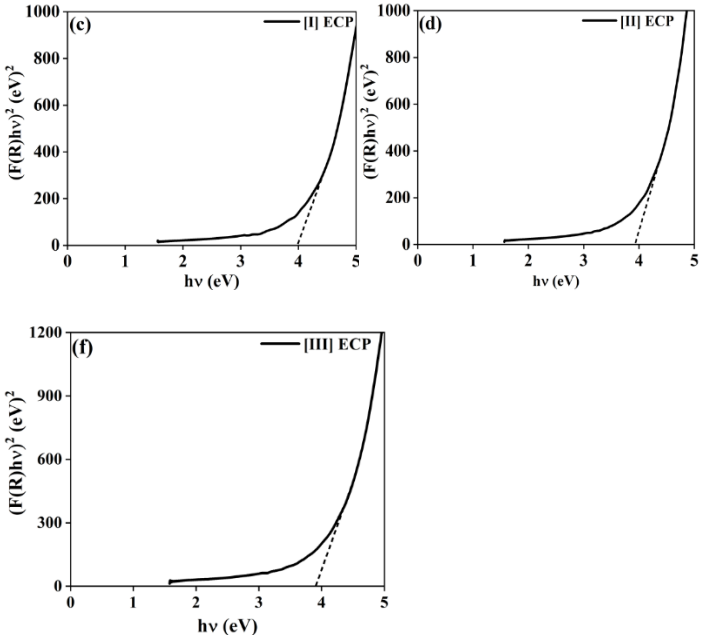

Figure 9: Plot of $(F(R)hu)^2$ as a function of photon energy (hu) for (a) CP, (b) Gr-ECP, (c) FGr-ECP [I], (d) FGr-ECP [II] and (e) FGr-ECP [III]

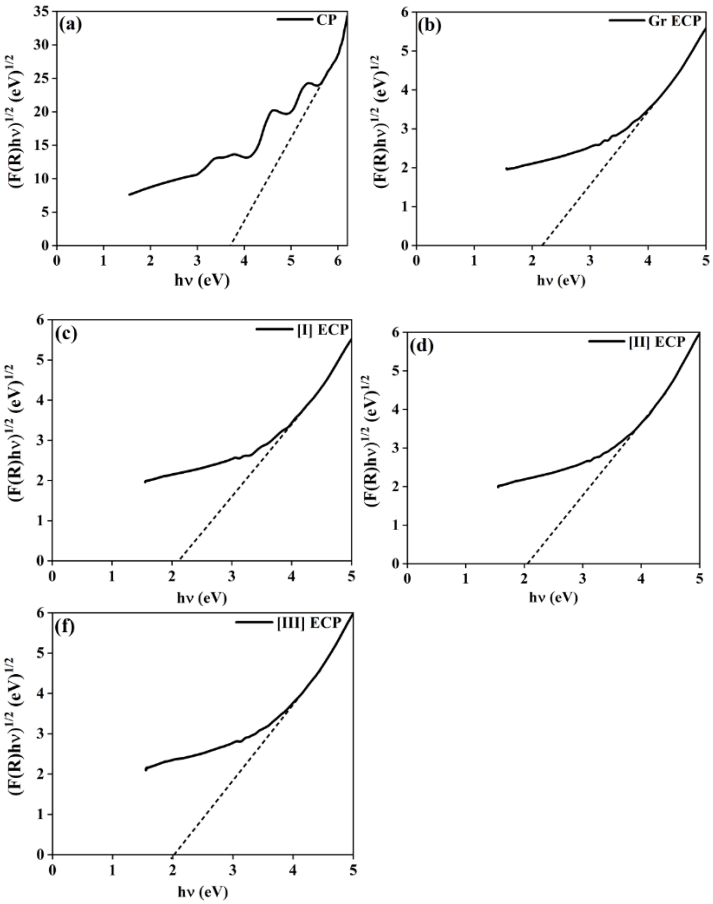

Figure 10: Plot of $(F(R)hu)^{1/2}$ as a function of photon energy (hu) for (a) CP, (b) Gr-ECP, (c) FGr-ECP [I], (d) FGr-ECP [II], and (e) FGr-ECP [III]

The above observations indicate the significance of FNPs over Gr coat ECPs. FNPs reduce the band gap of Gr-ECPs. The NCs have successfully served as a coating for cellulosic substrates to develop the ECP. FGr-ECP [III] indirect OBG (eV) value is 1.99, which is more significant than the other [I] and [II] FGr-ECP. The interaction between FNPs and Gr contributed to the π-π stacking interactions, which reduced the OBG of the composite.

Table 3: Direct and indirect OBG of ECPs.

Samples	Direct OBG (eV)	Indirect OBG (eV)
CP	5.27	3.70
Gr-ECP	3.99	2.15
FGr-ECP [I]	3.97	2.10
FGr-ECP [II]	3.91	2.04
FGr-ECP [III]	3.89	1.99

These interactions enhance charge carrier mobility and modify the electronic structure of Gr, leading to a narrowing of the band gap. The large surface area of Gr allows for the uniform dispersion of FNPs, creating a synergistic effect that improves charge transfer across the interface. This enhanced charge transfer contributes to lowering the energy barrier for electronic transitions, thereby reducing the band gap.

Conclusions

The present investigation explores the formation of nanocomposites (NCs) of ferrites with graphite coated on cellulose paper as a potential electrode material. FNP_S reduces the band gap after fabrication with graphite over CP (4 cm^2). ECP was fabricated by coating a Gr and HPMC composition with FNPs to formulate ferrite-graphite NCs coated over CP. TG-DTA-DTG reveals that NCs enhanced the thermal stability of the ECP. XRD data shows the mean crystallite size of FNPs to be 8.27 nm. The most intense peak in Gr is observed at 2θ=26.50°, revealing its

crystallite size as 30.79 nm. In the XRD pattern of FGr-ECP [III], the most intense peak is observed at 2θ=26.74°, attributed to a crystallite size of 33.37 nm. The increasing magnification from 10KX, 10 µm to 5KX, 5µm presents a smooth morphology of FGr-ECP [III]. Microanalysis reveals the proper stable coating of NCs over CP that was found homogeneous at 5KX, 5µm. The major decomposition of FGr-ECP [III] was observed in the 552 to 831 ^{o}C range with respective residual weights of 81.40 and 2.10 %. This range of decomposition was associated with a broad DTA signal of 0.22 at 554 ^{o}C, along with the heat of decomposition of -11.50 and DTG at the rate of 0.06 at 707 ^{o}C. Thermal characteristics reveal the potential of FNPs to modify the stability of NCs for the development of thermally stable ECPs. SEM image reveals a smooth surface of ECP that was phase-separated in the presence of FNPs. The concentration of FNPs and voltage has raised σDC of NCs to 0.011 S/cm at 100V. Ohmic behavior reveals the semiconducting nature of the coating. Reflectance Spectra, $F(R)hu)^2$ and $F(R)hu)^{1/2}$ as a function of photon energy (hu) indicate the significance of FNPs with Gr nanocomposite's (NCs) over ECPs contributed to the π-π stacking interactions on FGr-ECP [III] indirect OBG (eV) value is 1.99, giving a more significant outcome as compared to the other [I] and [II] FGr-ECP. An enhanced charge transfer contributes to lowering the energy barrier for electronic transitions, thereby reducing the band gap.

Acknowledgment: All authors acknowledge the management of Uttaranchal University, IIT Delhi, and NIT Kurukshetra for permitting and providing the infrastructural support. We are very thankful to the Bioinformatics Resources and Applications Facility (BRAF), C-DAC, Pune, for computational support.

Financial support: No financial support.

Potential conflicts of interest. The authors declare no conflict of interest.

References

Chang, B.Y. and Park, S.M., 2006. Integrated description of electrode/electrolyte interfaces based on equivalent circuits and its verification using impedance measurements. *Analytical chemistry*, *78*(4), pp.1052-1060.

Wang, F., Wu, X., Yuan, X., Liu, Z., Zhang, Y., Fu, L., Zhu, Y., Zhou, Q., Wu, Y. and Huang, W., 2017. Latest advances in supercapacitors: from new electrode materials to novel device designs. *Chemical Society Reviews*, *46*(22), pp.6816-6854.

Lizundia, E., Rincón-Iglesias, M. and Lanceros-Méndez, S., 2020. Combining cobalt ferrite and graphite with cellulose nanocrystals for magnetically active and electrically conducting mesoporous nanohybrids. *Carbohydrate polymers*, *236*, p.116001.

Oli, N., Flórez Gómez, J.F., Zuluaga Gómez, C.C., Katiyar, R.K., Morell, G. and Katiyar, R.S., 2023. Revealing Underestimated Performance in the Bismuth Ferrite (BiFeO3) Anode for High-Capacity and Long-Cycling Lithium-Ion Batteries. *ACS Applied Energy Materials*, *6*(21), pp.10853-10861.

Liu, Q., Chen, J., Li, Y., & Shi, G. (2016). High-performance strain sensors with fish-scale-like graphene-sensing layers for full-range detection of human motions. *ACS nano*, *10*(8), 7901-7906.

Zhang, T., Lv, D., Liu, R., Wang, D., Li, T., Xu, J., ... & Wang, L. (2021). Developing a superhydrophobic absorption-dominated electromagnetic shielding material by building clustered Fe3O4 nanoparticles on the copper-coated cellulose paper. *ACS Sustainable Chemistry & Engineering*, *9*(19), 6574-6585.

Sheberla, D., Bachman, J.C., Elias, J.S., Sun, C.J., Shao-Horn, Y. and Dincă, M., 2017. Conductive MOF electrodes for stable supercapacitors with high areal capacitance. *Nature materials*, *16*(2), pp.220-224.

Pereira, C., Costa, R. S., Lopes, L., Bachiller-Baeza, B., Rodríguez-Ramos, I., Guerrero-Ruiz, A., ... & Pereira, A. M. (2018). Multifunctional mixed valence N-doped CNT@ MFe 2 O 4 hybrid nanomaterials: from engineered one-pot coprecipitation to application in energy storage paper supercapacitors. *Nanoscale*, *10*(26), 12820-12840.

Lashkenari, M.S., Ghasemi, A.K., Khalid, M. and Shahgaldi, S., 2023. Facile synthesis of N-doped graphene oxide decorated with copper ferrite as an electrode material for supercapacitor with enhanced capacitance. *Electrochimica Acta*, *465*, p.142959.

Salama, R.S., Gouda, M.S., Aboud, M.F.A., Alshorifi, F.T., El-Hallag, A.A. and Badawi, A.K., 2024. Synthesis and characterization of magnesium ferrite-activated carbon composites derived from orange peels for enhanced supercapacitor performance. *Scientific Reports*, *14*(1), p.8223.

Hwang, G.H., Han, W.K., Park, J.S. and Kang, S.G., 2008. Determination of trace metals by anodic stripping voltammetry using a bismuth-modified carbon nanotube electrode. *Talanta*, *76*(2), pp.301-308.

Liang, L.Y., Liu, Z.M., Cao, H.T. and Pan, X.Q., 2010. Microstructural, optical, and electrical properties of SnO thin films prepared on quartz via a two-step method. *ACS applied materials & interfaces*, *2*(4),

pp.1060-1065.
Sethuraman, V.A., Srinivasan, V. and Newman, J., 2012. Analysis of electrochemical lithiation and delithiation kinetics in silicon. *Journal of the Electrochemical Society*, *160*(2), p. A394.
Peng, H.W., Yang, L.L., Lai, J.Q., Li, B., Liu, X.H. and Dai, Z.H., 2023. Mica geochemistry as an indicator of magmatic-hydrothermal processes in the Ta-Nb-Sn-W mineralization of the Limu deposit, South China. *Ore Geology Reviews*, *160*, p.105584.
Liu, Q., Chen, J., Li, Y. and Shi, G., 2016. High-performance strain sensors with fish-scale-like graphene-sensing layers for full-range detection of human motions. *ACS nano*, *10*(8), pp.7901-7906.
Nogi, M. and Yano, H., 2009. Optically transparent nanofiber sheets by deposition of transparent materials: A concept for a roll-to-roll processing. *Applied physics letters*, *94*(23).
Amin, K., Mao, L. and Wei, Z., 2019. Recent progress in polymeric carbonyl-based electrode materials for lithium and sodium ion batteries. *Macromolecular rapid communications*, *40*(1), p.1800565.
Ma, R., Chen, Z., Zhao, D., Zhang, X., Zhuo, J., Yin, Y., Wang, X., Yang, G. and Yi, F., 2021. Ti 3 C 2 T x MXene for electrode materials of supercapacitors. *Journal of Materials Chemistry A*, *9*(19), pp.11501-11529.
Norrman, K., Ghanbari-Siahkali, A. and Larsen, N.B., 2005. 6 Studies of spin-coated polymer films. *Annual Reports Section" C"(Physical Chemistry)*, *101*, pp.174-201.
Boccaccini, A.R., Cho, J., Roether, J.A., Thomas, B.J., Minay, E.J. and Shaffer, M.S., 2006. Electrophoretic deposition of carbon nanotubes. *Carbon*, *44*(15), pp.3149-3160.
Pollet, B.G. and Kalanur, S.S., 2024. Applications of Ferric Oxide in Water Splitting by Electrolysis: A Comprehensive Review. *Molecules*, *29*(21), p.4990.
Ghimire, U., Kandel, R., Ko, S.W., Adhikari, J.R., Kim, C.S. and Park, C.H., 2024. Electrochemical technique to develop surface-controlled polyaniline nano-tulips (PANINTs) on PCL-reinforced chitosan functionalized (CS-f-Fe2O3) scaffolds for stimulating osteoporotic bone regeneration. *International Journal of Biological Macromolecules*, *264*, p.130608.
Zhao, D., Zhu, Y., Cheng, W., Chen, W., Wu, Y. and Yu, H., 2021. Cellulose-based flexible functional materials for emerging intelligent electronics. *Advanced materials*, *33*(28), p.2000619.
Devi, G., Priya, R., Tapas Bapu, B.R., Thandaiah Prabu, R., Sathish Kumar, P.J. and Anusha, N., 2022. Role of carbonaceous fillers in electromagnetic interference shielding behavior of polymeric composites: A review. *Polymer Composites*, *43*(11), pp.7701-7723.
Sankaran, S., Deshmukh, K., Ahamed, M.B. and Pasha, S.K., 2018. Recent advances in electromagnetic interference shielding properties of metal and carbon filler reinforced flexible polymer composites: A review. *Composites Part A: Applied Science and Manufacturing*, *114*, pp.49-71.
Kausar, A., 2018. Contemporary applications of carbon black-filled polymer composites: An overview of essential aspects. *Journal of Plastic Film & Sheeting*, *34*(3), pp.256-299.
Tang, Y., Mosseler, J.A., He, Z. and Ni, Y., 2014. Imparting cellulosic paper of high conductivity by surface coating of dispersed graphite. *Industrial & Engineering Chemistry Research*, *53*(24), pp.10119-10124.
Hu, L., Choi, J.W., Yang, Y., Jeong, S., La Mantia, F., Cui, L.F. and Cui, Y., 2009. Highly conductive paper for energy-storage devices. *Proceedings of the National Academy of Sciences*, *106*(51), pp.21490-21494.
Gutiérrez, A., Alomari, N., Aparicio, S., Fleming, P.D., Pekarovicova, A., Wu, Q. and Atilhan, M., 2023. Understanding of three different polyvinylpyrrolidone (PVP) based battery binders blends on graphene surfaces from first principles via DFT simulations. *Materials Chemistry and Physics*, *301*, p.127548.
Jeong, S.S., Böckenfeld, N., Balducci, A., Winter, M. and Passerini, S., 2012. Natural cellulose as binder for lithium battery electrodes. *Journal of Power Sources*, *199*, pp.331-335.
Hina, M., Bashir, S., Kamran, K., Almomani, F., Ahmad, J., Kamarulazam, F., Ramesh, S., Ramesh, K. and Mujtaba, M.A., 2024. Energy storage devices based on flexible and self-healable hydrogel electrolytes: Recent advances and future prospects. *Journal of Energy Storage*, *85*, p.110961.
Kasprzak, D., Mayorga-Martinez, C.C. and Pumera, M., 2022. Sustainable and flexible energy storage devices: a review. *Energy & Fuels*, *37*(1), pp.74-97.
Ji, L., Chen, W., Xu, Z., Zheng, S. and Zhu, D., 2013. Graphene nanosheets and graphite oxide as promising adsorbents for removal of organic contaminants from aqueous solution. *Journal of environmental quality*, *42*(1), pp.191-198.
Ivancev-Tumbas, I., Landwehrkamp, L., Hobby, R., Vernillo, M. and Panglisch, S., 2020. Adsorption of organic pollutants from the aqueous phase using graphite as a model adsorbent. *Adsorption Science & Technology*, *38*(7-8), pp.286-303.
Li, S., Liu, Y.M., Zhang, Y.C., Song, Y., Wang, G.K., Liu, Y.X., Wu, Z.G., Zhong, B.H., Zhong, Y.J. and Guo, X.D., 2021. A review of rational design and investigation of binders applied in silicon-based anodes for lithium-ion batteries. *Journal of Power Sources*, *485*, p.229331.
Zhao, Y., Li, X., Yan, B., Xiong, D., Li, D., Lawes, S. and Sun, X., 2016. Recent developments and understanding of novel mixed transition-metal oxides as anodes in lithium ion batteries. *Advanced Energy Materials*, *6*(8), p.1502175.
Zhou, G., Wang, D.W., Li, F., Zhang, L., Li, N., Wu, Z.S., Wen, L., Lu, G.Q. and Cheng, H.M., 2010. Graphene-wrapped Fe3O4 anode material with improved reversible capacity and cyclic stability for lithium ion batteries. *Chemistry of materials*, *22*(18), pp.5306-5313.
Nongjai, R., Khan, S., Asokan, K., Ahmed, H. and Khan, I., 2012. Magnetic and electrical properties of In doped

cobalt ferrite nanoparticles. *Journal of applied physics*, *112*(8).

Hashim, A., Agool, I.R. and Kadhim, K.J., 2018. Novel of (polymer blend-Fe3O4) magnetic nanocomposites: preparation and characterization for thermal energy storage and release, gamma ray shielding, antibacterial activity and humidity sensors applications. *Journal of Materials Science: Materials in Electronics*, *29*(12), pp.10369-10394.

Rana, G., Dhiman, P., Kumar, A., Vo, D.V.N., Sharma, G., Sharma, S. and Naushad, M., 2021. Recent advances on nickel nano-ferrite: A review on processing techniques, properties and diverse applications. *Chemical Engineering Research and Design*, *175*, pp.182-208.

Qin, H., He, Y., Xu, P., Huang, D., Wang, Z., Wang, H., Wang, Z., Zhao, Y., Tian, Q. and Wang, C., 2021. Spinel ferrites (MFe2O4): Synthesis, improvement and catalytic application in environment and energy field. *Advances in Colloid and Interface Science*, *294*, p.102486.

Nawwar, M., Poon, R., Chen, R., Sahu, R.P., Puri, I.K. and Zhitomirsky, I., 2019. High areal capacitance of Fe3O4-decorated carbon nanotubes for supercapacitor electrodes. *Carbon Energy*, *1*(1), pp.124-133.

Bruck, A.M., Cama, C.A., Gannett, C.N., Marschilok, A.C., Takeuchi, E.S. and Takeuchi, K.J., 2016. Nanocrystalline iron oxide based electroactive materials in lithium ion batteries: the critical role of crystallite size, morphology, and electrode heterostructure on battery relevant electrochemistry. *Inorganic Chemistry Frontiers*, *3*(1), pp.26-40.

Zhang, T. and Ran, F., 2021. Design strategies of 3D carbon-based electrodes for charge/ion transport in lithium ion battery and sodium ion battery. *Advanced Functional Materials*, *31*(17), p.2010041.

Sumdani, M.G., Islam, M.R., Yahaya, A.N.A. and Safie, S.I., 2022. Recent advancements in synthesis, properties, and applications of conductive polymers for electrochemical energy storage devices: A review. *Polymer Engineering & Science*, *62*(2), pp.269-303.

Anwar, M., Cochran, E.W., Zulfiqar, S., Warsi, M.F., Shakir, I. and Chaudhary, K., 2023. In-situ fabricated copper-holmium co-doped cobalt ferrite nanocomposite with cross-linked graphene as novel electrode material for supercapacitor application. *Journal of Energy Storage*, *72*, p.108438.

Tashakkorian, H., Aflatoonian, B., Jahani, P.M. and Aflatoonian, M.R., 2022. Electrochemical sensor for determination of hydroxylamine using functionalized Fe_3O_4nanoparticles and graphene oxide modified screen-printed electrode. *Journal of Electrochemical Science and Engineering*, *12*(1), pp.71-79.

Tang, Y., He, Z., Mosseler, J.A. and Ni, Y., 2014. Production of highly electro-conductive cellulosic paper via surface coating of carbon nanotube/graphene oxide nanocomposites using nanocrystalline cellulose as a binder. *Cellulose*, *21*, pp.4569-4581.

Lizundia, E., Rincón-Iglesias, M. and Lanceros-Méndez, S., 2020. Combining cobalt ferrite and graphite with cellulose nanocrystals for magnetically active and electrically conducting mesoporous nanohybrids. *Carbohydrate polymers*, *236*, p.116001.

Scherrer, P., 1918. Bestimmung der Grosse und inneren Struktur von Kolloidteilchen mittels Rontgenstrahlen. *Nach Ges Wiss Gottingen*, *2*, pp.8-100.

Fatimah, S., Ragadhita, R., Al Husaeni, D.F. and Nandiyanto, A.B.D., 2022. How to calculate crystallite size from x-ray diffraction (XRD) using Scherrer method. *ASEAN Journal of Science and Engineering*, *2*(1), pp.65-76.

Tauc, J., 1974. Optical properties of amorphous semiconductors. In *Amorphous and liquid semiconductors* (pp. 159-220). Boston, MA: Springer US.

López-Caravaca, A., Nicolás, J.F., Lucarelli, F., Castaner, R., Crespo, J., Galindo, N., Calzolai, G., Yubero, E., Clemente, A. and Pazzi, G., 2022. Combination of PM optical and chemical properties to estimate the contribution of non-BC absorbers to light absorption at a remote site. *Atmospheric Research*, *268*, p.106000.

Ma, C., Yang, K., Wang, L. and Wang, X., 2017. Facile synthesis of reduced graphene oxide/Fe3O4 nanocomposite film. *Journal of Applied Biomaterials & Functional Materials*, *15*(1_suppl), pp.1-6.

Costa, M.N., Veigas, B., Jacob, J.M., Santos, D.S., Gomes, J., Baptista, P.V., Martins, R., Inácio, J. and Fortunato, E., 2014. A low cost, safe, disposable, rapid and self-sustainable paper-based platform for diagnostic testing: lab-on-paper. *Nanotechnology*, *25*(9), p.094006.

Jain, R., 2022. A review on the development of XRD in ferrite nanoparticles. *Journal of Superconductivity and Novel Magnetism*, *35*(5), pp.1033-1047.

TODICA, M., Stefan, T., Simon, S., Balasz, I. and Daraban, L., 2014. UV-Vis and XRD investigation of graphite-doped poly (acrylic) acid membranes. *Turkish Journal of Physics*, *38*(2), pp.261-267.

Verma, M., Naqvi, T.K., Tripathi, S.K., Kulkarni, M.M. and Dwivedi, P.K., 2021. Paper based low-cost flexible SERS sensor for food adulterant detection. *Environmental Technology & Innovation*, *24*, p.102033.

Mani, N.K., Prabhu, A., Biswas, S.K. and Chakraborty, S., 2019. Fabricating paper based devices using correction pens. *Scientific Reports*, *9*(1), p.1752.

Zhang, J., Li, Z., Zhang, C., Feng, B., Zhou, Z., Bai, Y. and Liu, H., 2012. Graphite-coated paper as substrate for high sensitivity analysis in ambient surface-assisted laser desorption/ionization mass spectrometry. *Analytical chemistry*, *84*(7), pp.3296-3301.

Han, H., Jiang, C., Huo, L. and Gao, J., 2016. Mechanical and thermal properties of cationic ring-opening o-cresol formaldehyde epoxy/polyurethane acrylate composites enhanced by reducing graphene oxide. *Polymer Bulletin*, *73*, pp.2227-2244.

Zygouri, P., Spyrou, K., Papayannis, D.K., Asimakopoulos, G., Dounousi, E., Stamatis, H., Gournis, D. and Rudolf, P., 2022. Comparative study of various graphene oxide structures as efficient drug release systems for ibuprofen. *AppliedChem*, *2*(2), pp.93-105.

Chan, E.M., 2015. Combinatorial approaches for developing upconverting nanomaterials: high-throughput screening, modeling, and applications. *Chemical Society Reviews*, *44*(6), pp.1653-1679.

Persano, F., Batasheva, S., Fakhrullina, G., Gigli, G., Leporatti, S. and Fakhrullin, R., 2021. Recent advances in the design of inorganic and nano-clay particles for the treatment of brain disorders. *Journal of Materials Chemistry B*, *9*(12), pp.2756-2784.

Mund, H.S., Prajapat, P., Dhaka, S., Kumar, S., Saxena, A. and Meena, S.S., 2021. Impact of annealing temperature on structural, optical, and Mössbauer properties of nanocrystalline NiFe2O4. *Journal of Materials Science: Materials in Electronics*, *32*(23), pp.27232-27242.

Jalil, M.A., Chowdhury, S.S., Alam Sakib, M., Enamul Hoque Yousuf, S.M., Khan Ashik, E., Firoz, S.H. and Basith, M.A., 2017. Temperature-dependent phase transition and comparative investigation on enhanced magnetic and optical properties between sillenite and perovskite bismuth ferrite-rGO nanocomposites. *Journal of Applied Physics*, *122*(8).

Ahmed, K.K., Muheddin, D.Q., Mohammed, P.A., Ezat, G.S., Murad, A.R., Ahmed, B.Y., Hussen, S.A., Ahmed, T.Y., Hamad, S.M., Abdullah, O.G. and Aziz, S.B., 2024. A brief review on optical properties of polymer composites: insights into light-matter interaction from classical to quantum transport point of view. *Results in Physics*, *56*, p.107239.